Online Dielectric Response Analysis under Mixed-Frequency Medium-Voltage Stress

Author(s):
Färber, Raphael; Franck, Christian

Publication date:
2019

Permanent link:
https://doi.org/10.3929/ethz-b-000341625

Originally published in:
Lecture Notes in Electrical Engineering 599, https://doi.org/10.1007/978-3-030-31680-8_105

ONLINE DIELECTRIC RESPONSE ANALYSIS UNDER MIXED-FREQUENCY MEDIUM-VOLTAGE STRESS

R. Färber*, A. Nasef and C.M. Franck
High Voltage Laboratory, ETH Zürich, Physikstrasse 3, Switzerland
*Email: faerberr@ethz.ch

Abstract: A custom-made dielectric spectrometer using the broadband excitation of pulse-width-modulated medium-voltages is presented and its performance assessed. A simple technique is suggested and validated for eliminating the problem associated with the digitization of capacitive currents with large crest factors, which arise with rectangular excitation voltages. The developed system allows a quasi-continuous monitoring of the dielectric spectrum (time resolution ~1 s, frequency range ~1 kHz to 100 kHz) of insulation specimens exposed to mixed-frequency voltages, and thus represents a promising tool for insulation aging studies under these non-conventional high-voltage stress profiles.

1 INTRODUCTION

The dielectric spectrum of an insulating material provides a rich source of information about the dynamics of its constituent (bound and mobile) electrical charge carriers. Thus, it is potentially susceptible to stress-induced changes of a specimen's molecular structure. Consequently, dielectric spectroscopy has found widespread application in insulation aging studies [1, 2]. Under high-voltage stress (>1 kV), however, the excitation voltage is typically limited to a sinusoidal waveform [3, 4]. While non-sinusoidal excitations *are* widely used in impedance spectroscopy, these systems do not operate in the high-voltage regime, or suffer from other constraints such as limited excitation voltage bandwidth, the inability to survive test object breakdown or the need for elaborate measurement circuit modelling [5].

In this paper, an online dielectric spectrometer setup for mixed-frequency voltages up to 30 kV is presented. It is immune against test object breakdown, employs analog signal processing to remove the limitation on the rate of rise of voltage, and uses a referencing technique to avoid the need for modelling. It is therefore suitable to complement time-to-failure testing of insulation materials under medium-voltage inverter waveforms, providing in-situ measurements of the pre-breakdown dynamics of the dielectric spectrum. As such, it constitutes a promising tool for further illumination of the active degradation mechanisms in insulation systems exposed to mixed-frequency medium-voltages (e.g. DC-biased rectangular voltages), both above and – in particular – below partial discharge inception [6].

The paper is organized as follows. First, detailed information about the excitation voltage used in this study, as well as the analog and digital signal processing employed for determining the dielectric permittivity is provided. Then, the dielectric spectrometer is characterized based on its precision, accuracy and stability. Finally, a proof of concept measurement is shown and discussed.

2 METHODS

The measurement setup as well as parameter definitions and theoretical concepts used in the result section are detailed in Subsections 2.1 to 2.4.

2.1 Voltage source

The online dielectric spectrometer was designed to operate on a mixed-frequency test bench, whose schematic is shown in Figure 1a. The sample inside the test cell can be stressed by a DC voltage U_{DC} (0 to 30 kV) and a superimposed medium-frequency rectangular pulse voltage U_p (0 to 1.5 kV peak-peak, with a fundamental frequency between 500 Hz and 10 kHz). A more detailed description of the test bench as well as results on time-to-failure testing under this stress profile can be found in [6].

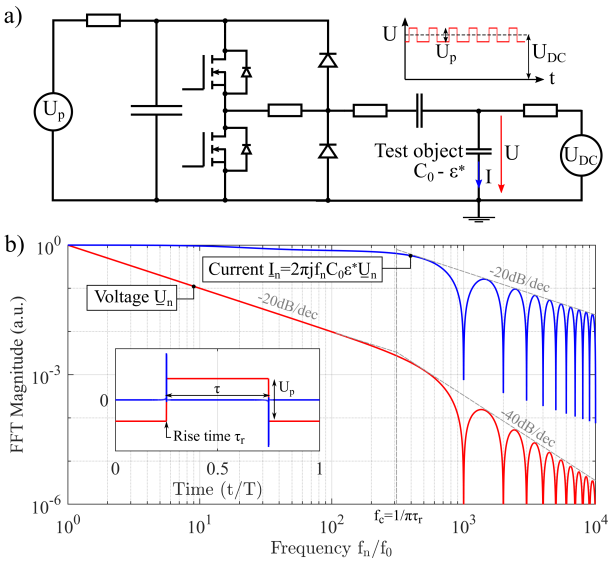

Figure 1: a) Simplified schematic of the test bench used to apply DC-biased medium-frequency rectangular pulse voltages to the test object, characterized by a vacuum capacitance C_0 and its dielectric permittivity ε^*. b) Spectrum of the applied trapezoidal pulse train and the corresponding response current through the test object.

2.2 Spectrum of a trapezoidal pulse train

The Fourier components of a trapezoidal pulse of fundamental period T, pulse length τ (full width at half maximum), rise time τ_r and peak-to-peak amplitude U_p can be calculated to be

$$\underline{U}_n = 2\,U_p\,\frac{\tau}{T}\,\mathrm{sinc}(\pi f_n \tau_r)\,\mathrm{sinc}(\pi f_n \tau), \qquad (1)$$

with $f_n = n/T$ and $n = 1,2,3,\ldots$ (DC component not considered). The associated time-domain waveform reads

$$U(t) = \mathrm{Re}\left[\sum_{n=1}^{\infty} \underline{U}_n e^{2\pi j f_n t}\right] \qquad (2)$$

The summation becomes finite for bandwidth-limited signals, e.g. digitized voltages $U_m = U(t_m)$ with $t_m = m/f_s$ ($m = 0,1,2,\ldots$), for which the highest frequency is half the sampling frequency f_s (= Nyquist frequency). The envelope of the trapezoidal pulse spectrum is obtained by observing that the envelope of the $\mathrm{sinc}(x)$ function is approximately 1 for $x \lesssim 1$ and x^{-1} for $x \gtrsim 1$. Thus the pulse envelope is constant ($= 2U_p\tau/T$) for $f_n \lesssim 1/\pi\tau$, decreasing as f_n^{-1} (−20 dB/dec) for $1/\pi\tau \lesssim f_n \lesssim 1/\pi\tau_r \equiv f_c$ and dropping off as f_n^{-2} (−40 dB/dec) for $f_n \gtrsim f_c$. The spectral components of a pulse train with duty cycle $D = \tau/T = 0.5$ and $\tau_r = 10^{-3}T$ is shown in Figure 1b (note that a significant constant regime is only present if $D \ll 1$). The frequency range $[f_0, f_c]$ contains 99.97% of the spectral power, and hence the spectral contribution above f_c can usually be neglected for, e.g., dielectric loss calculations.

The current flowing through a capacitor with a linear and isotropic dielectric characterized by the complex dielectric permittivity $\varepsilon_n^* = \varepsilon^*(f_n)$ is given by

$$I(t) = C_0\,\mathrm{Re}\left[\sum_{n=1}^{\infty} 2\pi j f_n \varepsilon_n^* \underline{U}_n e^{2\pi j f_n t}\right] \qquad (3)$$

The corresponding Fourier amplitudes are also shown in Figure 1b. The complex permittivity in the given example is modelled by a Debye relaxation

$$\varepsilon^*(f) = \varepsilon_\infty + \frac{\Delta\varepsilon}{1+2\pi j f/f_{rel}} = 3 + \frac{1}{1+2\pi j f/(20\cdot f_0)}. \qquad (4)$$

It causes the current components to decrease by a factor $1 + \Delta\varepsilon/\varepsilon_\infty \approx 1.3$ when the frequency changes from $f \ll f_{rel}$ to $f_{rel} \ll f \lesssim f_c$. For a given excitation voltage, the current response contains – in principle – all the information about the dielectric permittivity as defined above. If the vacuum capacitance C_0 is known, ε^* can be evaluated at all "measureable" harmonics of the excitation voltage by using

$$\varepsilon_n^* = \left[2\pi j f_n C_0 \underline{U}_n/\underline{I}_n\right]^{-1}. \qquad (5)$$

The crux of the matter lies in the limited ability to experimentally determine the Fourier coefficients with sufficient precision and accuracy.

2.3 Signal conditioning and digitization

Dielectric spectroscopy relies on a precise measurement of the applied excitation voltage and the associated sample current. A signal processing procedure optimized for rectangular voltage excitation is presented in the following subsections.

2.3.1 Voltage measurement

In order to increase the signal to noise ratio, a custom-made voltage divider with a band-pass characteristic as shown in Figure 2 is employed to measure the AC voltage applied to the specimen. The pass band corner frequencies are set to 500 Hz and 100 kHz, which is deemed a suitable compromise between system bandwidth and noise performance for the available pulse excitation frequencies. This range can be adjusted to match other excitation spectra by modifying the filter component values. The full transfer from the applied high voltage $\underline{U}_{HV}$ to the digitized low voltage $\underline{U}_{out}^{(1)}$ can – under the assumption of system linearity – be written as

$$\underline{U}_{out}^{(1)} = \frac{C_{HV}}{C_{LV}}\underline{T}^{(1)}\underline{U}_{HV} \equiv \underline{U}_{HV}/\underline{\alpha}^{(1)}. \qquad (6)$$

The divider ratio in the pass band is given by

$$r = \left|\underline{\alpha}^{(1)}\right| = \frac{100\mathrm{nF}}{100\mathrm{pF}} \cdot \frac{1}{4\mathrm{V/V}} = 250. \qquad (7)$$

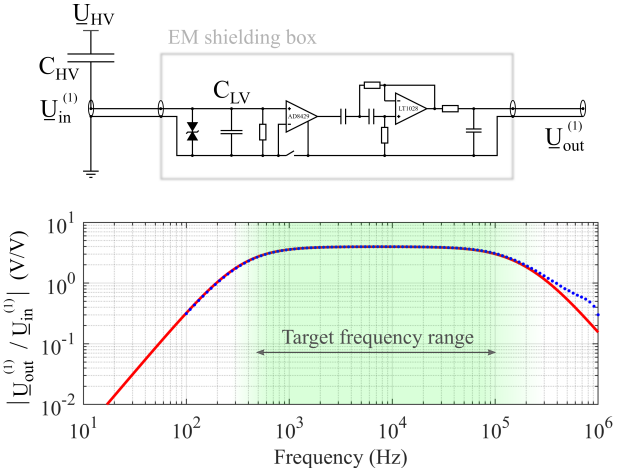

Figure 2: Simplified schematic of the voltage divider signal conditioner and the corresponding transfer function (simulated − vs. measured ···).

2.3.2 Current measurement

The crest factor (CF) of a periodic signal is defined as the ratio of its peak value to its RMS value. While for the trapezoidal voltage $CF_U \approx 1$ (assuming $\tau \approx T/2$ and $\tau_r \ll T$), the associated capacitive current features $CF_I \approx \sqrt{T/2\tau_r} \gg 1$. For a given spectral content of a signal (i.e. given Fourier *magnitudes*), a higher crest factor leads to a higher quantization noise during analog-to-digital conversion (ADC) and hence a smaller S/N ratio for the spectral components. Indeed, for a given set of magnitudes $\{\hat{A}_n \geq 0, n \in \mathbb{N}\}$ with $\sum_n^\infty \sqrt{2}\hat{A}_n^2 = A_{RMS} = 1$, consider the set of signals $\{\underline{A}_n^{(i)} = \hat{A}_n e^{j\phi_n^{(i)}},\ \phi_n \in [0,2\pi)\}$. While the RMS value of all these signals is the same, the peak values $A_{peak}^{(i)}$ are functions of the phases $\phi_n^{(i)}$. Let $A_{peak}^{min} = CF_A^{min}$ be the infimum of all

peak values, and $A_{peak}^{max} = \sum \hat{A}_n = CF_A^{max}$ their maximum. Hence, when digitizing with N_b bits, the largest and smallest digitization quanta are given by

$$\Delta A^{max/min} \geq CF_A^{max/min}/2^{N_b} \quad (8)$$

(equality applies when the reference value for the quantization is optimal, i.e. equal to the peak value of the signal). It is thus clear that in order to utilize best the available vertical resolution of the ADC, one should avoid large crest factors of the analog input signals.

In order to reduce the current signal's large crest factor $CF_I \approx \sqrt{T/2\tau_r}$ (e.g. equal to 71 for T=1 ms and τ_r=100 ns), an analog integration of the signal is performed before digitization. The resulting crest factors are much smaller ($\lesssim$2) and thus the signal can be digitized without sacrificing more than one bit of the ADC's dynamic range (instead of sacrificing more than six bits with a crest factor of 71). Numerical simulation shows the instrument precision for both magnitude and phase to scale strongly with the number of digitization bits: $A \sim e^{-a \cdot N_b}$ with $a \approx 0.6$ (this of course only applies if the noise level at the ADC inputs is lower than the quantization noise associated with N_b). Saving 5 bits of resolution thus amounts to an order of magnitude improvement on precision.

Figure 3 shows the schematic of the designed integrator and its transfer function $\underline{T}^{(2)}$, which features the integrating behaviour $\sim[jf]^{-1}$ within the target frequency range between about 500 Hz and 100 kHz. The full transfer from the sample current I_s to the digitized voltage reads

$$\underline{U}_{out}^{(2)} = \underline{T}^{(CT)}\underline{T}^{(2)}\underline{I}_S \equiv \underline{I}_S/\underline{\alpha}^{(2)}, \quad (9)$$

where $\underline{T}^{(CT)}$ is the transfer function of the current transformer. The one used in this application features a lower −3 dB cutoff at about 300 Hz and a flat response (1 V/A) in the target frequency range.

In addition to ensuring good utilization of the ADC's dynamic range, using an integrator also matches the S/N ratio of the current harmonics to those of the voltage signal. Specifically, prior to implementing integration, the S/N ratios of the current harmonics are approximately constant (assuming a constant noise floor), while after integration they decrease with the inverse of the frequency (as they do for the voltage harmonics).

2.3.3 Digitization and Fourier transform

The voltages $U_{out}^{(1,2)}(t)$ are digitized by using a 16-bit ADC with a maximum sampling frequency f_s of 6.25 MHz. Frequencies that could be aliased onto a frequency in the target range are suppressed by the transfer functions with −60 dB or more with respect to the target frequency. A Fast Fourier Transform is performed on a pulse train containing 100 fundamental cycles in order to determine the spectral components $\underline{U}_{out}^{(1,2)}$. Spectral leakage is reduced by applying a Hanning window.

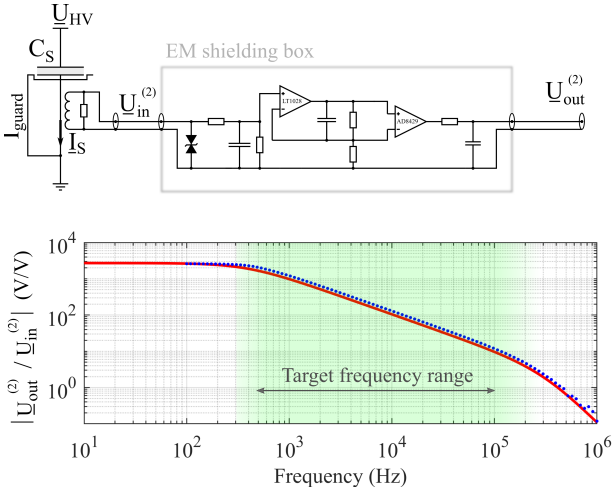

Figure 3: Simplified schematic of the voltage integrator and its transfer function (simulated − vs. measured ···). The voltage integrator is fed by a current transformer (1 V/A) measuring the alternating current I_S flowing through the sample capacitance C_S.

2.4 Definition of instrument precision

Let $\{x_i, i = 1, \ldots, N\}$ be $N > 1$ measured values (e.g. the magnitude or phase of the permittivity at a certain frequency). Assume that it is a sample of a random variable X distributed according to a probability distribution f, whose mean value and standard deviation are denoted by μ and σ, respectively. For a given confidence level α, let the quantity A be the smallest real number satisfying

$$P(|X - \mu| \geq A/2) \leq 1 - \alpha. \quad (10)$$

For example, for $\alpha = 95\%$ Equation (10) asserts that the probability of a measured value lying outside $\mu \pm A/2$ is $\leq 1 - \alpha = 5\%$. In the present context, for given instrument settings, we thus call A the α-*precision* of the instrument with respect to the measured parameter. Unless stated otherwise, $\alpha = 95\%$ is assumed in the following.

A is conveniently expressed in units of standard deviations: $A_k = k \cdot \sigma$. Chebyshev's inequality then provides the distribution-independent precision $k = 2/\sqrt{1-\alpha} \approx 9$. Making the assumption that the distribution of X is symmetrical and unimodal [7] leads to a precision $k = 4/3\sqrt{\alpha} \approx 6$. The familiar stronger bound $k \approx 4$ ("95% of the measurements lie within two standard deviations of the mean") requires X to be normally distributed.

Since the standard deviation σ is unknown, it must be estimated from the measured sample:

$$\sigma_N = \sqrt{\Sigma_{n=1}^{N}(x_i - \mu_N)^2/(N-1)} \quad (11)$$

Its upper α-confidence bound in units of the estimator σ_N is given by [8]

$$u_N = \sqrt{\frac{N-1}{\chi_{(\alpha/2,N-1)}}} \qquad (12)$$

where $\chi_{(\alpha/2,N-1)}$ is the percentile of the Chi-Squared distribution. The instrument precision, based on the sample $\{x_i\}$, is thus given by $A = k \cdot u_N \cdot \sigma_N$.

The instrument precision (providing probabilistic bounds on the outcome of a *single* measurement) is different from the *confidence interval on the mean value* μ_N of N measurements ($\mu_N = N^{-1}\sum_{i=1}^{N} x_i$). The latter is given by $\mu_N \pm t_{(\alpha/2,N-1)}\sigma_N/\sqrt{N}$, where $t_{(\alpha/2,N-1)}$ is the percentile of Student's t distribution. The implicit central limit theorem requires $N \gg 1$ (in practice the approximation is good for $N \geq 10$).

2.5 Calculating the dielectric permittivity

For an electrode configuration of vacuum capacitance C_0 the (effective) complex dielectric permittivity of the sample is – by definition – related to the measured impedance by

$$\varepsilon^* = \varepsilon' - j\varepsilon'' = |\varepsilon^*|e^{-j\delta} = \left[2\pi j f C_0 \underline{Z}_S\right]^{-1}. \qquad (13)$$

Equations (6) and (9) yield

$$\underline{Z}_S = \frac{\underline{U}_{HV,S}}{\underline{I}_S} = \frac{\underline{\alpha}_S^{(1)}\underline{U}_{out,S}^{(1)}}{\underline{\alpha}_S^{(2)}\underline{U}_{out,S}^{(2)}}, \qquad (14)$$

where $\underline{\alpha}_S^{(1,2)}$ are the transfer functions (described in sections 2.3.1 and 2.3.2) applying at the instant of the measurement. Performing a "reference measurement" is a practical way for eliminating the unknown transfer functions [2]. Let $\underline{Z}_R$ be the impedance of a "reference sample":

$$\underline{Z}_R = \frac{\underline{U}_{HV,R}}{\underline{I}_R} = \frac{\underline{\alpha}_R^{(1)}\underline{U}_{out,R}^{(1)}}{\underline{\alpha}_R^{(2)}\underline{U}_{out,R}^{(2)}}. \qquad (15)$$

Under the assumption of equal transfer at the moment of the sample (S) and reference (R) measurements (the validity of this assumption will be discussed in section 4),

$$\underline{\alpha}_S^{(i)} = \underline{\alpha}_R^{(i)} \quad (i = 1,2), \qquad (16)$$

one obtains

$$\frac{\varepsilon_S^*}{\varepsilon_R^*} = \frac{C_{0,R}}{C_{0,S}} \cdot \frac{\underline{Z}_R}{\underline{Z}_S} = \frac{C_{0,R}}{C_{0,S}} \cdot \frac{\underline{U}_{out,S}^{(2)}\underline{U}_{out,R}^{(1)}}{\underline{U}_{out,S}^{(1)}\underline{U}_{out,R}^{(2)}}. \qquad (17)$$

The reference sample may be an air capacitor, in which case $\varepsilon_R^* = 1$ and thus Equation (17) provides the complex permittivity of the sample in terms of measured voltages and vacuum capacitances.

Alternatively, using the sample itself as a reference is an interesting choice for aging experiments. Equation (17) then reads

$$\frac{\varepsilon^*(t)}{\varepsilon^*(t_0)} = \frac{\underline{U}_{out}^{(2)}(t)\,\underline{U}_{out}^{(1)}(t_0)}{\underline{U}_{out}^{(1)}(t)\,\underline{U}_{out}^{(2)}(t_0)} \qquad (18)$$

and provides the time evolution of the complex permittivity as compared to its value at some time t_0 (e.g. the permittivity of the unaged material).

3 RESULTS

The results section presents data characterizing the measurement setup (accuracy / precision / stability) as well as a proof-of-concept measurement assessing its applicability on actual dielectric samples subject to electrical field stressing.

3.1 Instrument accuracy – Debye sample

In order to validate the basic operating principle of the setup and to assess its accuracy, the frequency-dependent permittivity of a Debye network,

$$\varepsilon^*_{Debye} = \frac{\underline{Z}_{Debye(C_1=0)}}{\underline{Z}_{Debye}} = 1 + \frac{C_1/C_0}{1+2\pi j f R_1 C_1}, \qquad (19)$$

is measured by using the reference principle (see Equation 17). The nominal component values are C_0=700 pF, C_1=220 pF and R_1=60 kΩ. A relatively low excitation voltage of 150 V (peak) is chosen for this sample in order to match the current amplitude to those expected for "real" material samples (for which the capacitance is in the range of 5 to 100 pF). A rectangular pulse train voltage excitation with a fundamental frequency of 1 kHz and a rise time of 100 ns is used. The magnitude and phase of the permittivity are determined from 1 kHz to 100 kHz and compared to the expected frequency response given by Equation (19). A linear frequency axis is chosen because the square wave harmonics $(2n+1)f_0$ are equidistant on this scale.

The lumped circuit components are treated as ideal, which is a valid approximation in the considered frequency range. For example, the loss factor of the used capacitors is ≤ 10^{-4}, which is much smaller than the maximum value (0.14) of the constructed Debye sample.

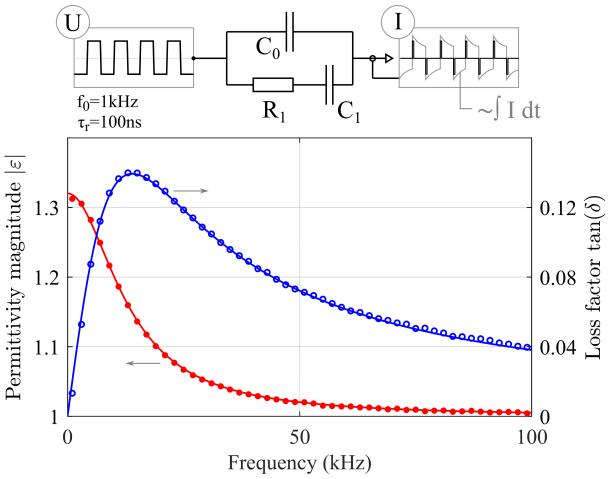

Figure 4: Validation of the measurement principle on a Debye network of known frequency response. Continuous lines are theoretical predictions based on Equation (19). Measured values (circles) are extracted from the harmonics of the square wave excitation and the corresponding current response.

3.2 Instrument precision and stability

The instrument precision A is calculated as defined in Section 2.4, using $\alpha = 0.95$, $N = 100$, $k = 6$ and $u_{100} = 1.16$, which yields $A \approx 7 \cdot \sigma_{100}$. As illustrated in Figure 5, averaging the outcome of N consecutive measurements reduces the scatter of the average value (at the expense of temporal resolution).

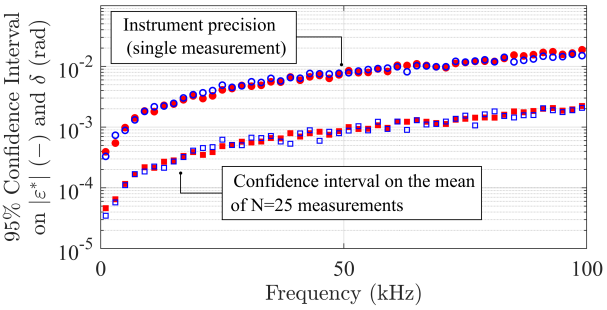

Figure 5: 95% confidence intervals on single measurements (instrument precision) and the mean of 25 measurements. Filled markers: permittivity magnitude, unfilled markers: phase angle (in rad).

The long-term stability of the output readings was evaluated by measurements on a commercial 50 kV ceramic capacitor for which no significant changes of the dielectric are expected. The DC voltage was increased step-wise up to 10 kV (1 kV every 2 minutes) with a superimposed U_p = 0.75 kV (peak-peak) / f_0 = 1 kHz / τ_r = 100 ns rectangular pulse train. Over a period of one hour (the maximal measurement time for the tests presented in this paper) the measured values of the magnitude and the phase of the permittivity are observed to fluctuate within a band of ≤ 10^{-3} and ≤ $2 \cdot 10^{-4}$ rad, respectively. These values are thus taken as thresholds below which measured changes are not attributed to the test object.

3.3 Pre-breakdown evolution of permittivity

A sample made of biaxially oriented PET foil (Melinex® S, 23 µm) is subject to a DC-biased rectangular pulse voltage. The electrodes (D=10 mm) consist of silver paint. The sample is conditioned and tested at T = 25±1 °C and RH = 33±2 %.

Figure 6 represents the time evolution of the normalized permittivity (Equation 18) when the sample is stressed with a step-wise increasing DC voltage U_{DC}, superimposed by a 0.75 kV / 1 kHz / 100 ns rectangular pulse train. A full spectrum is acquired every 6 seconds. For t>22 minutes the DC voltage is kept at 10 kV until breakdown occurs. While both the measured magnitude and phase change as a function of U_{DC}, sample breakdown is not preceded by any detectable abnormality. While the magnitude shows no significant change at all (<10^{-3}) prior to breakdown, the phase decreases slightly from its maximal value by about 10^{-3} rad across all frequencies.

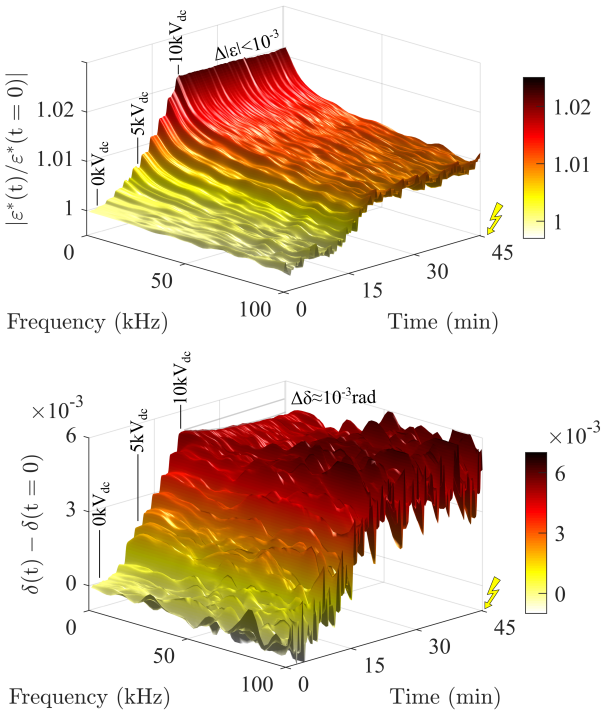

Figure 6: Time evolution of the absolute value (top) and the phase angle (bottom) of the normalized dielectric permittivity when the DC-bias voltage is increased in 1 kV steps from 0 to 10 kV (within 22 minutes) until breakdown occurs at t = 47 minutes.

4 DISCUSSION

The observation that the dielectric spectrum of the tested PET foil does not show any peculiarities prior to breakdown was surprising at first. However, on the one-hour time scale used here, electric field-induced changes are not expected to occur in a significant fraction of the sample's volume, i.e. properly speaking there is no electrical aging of the bulk material. The measurement suggests that during the time prior to breakdown, the processes occurring at a potential breakdown site are so localized that they do not alter the dielectric response of the sample. It is however important to note that *some* internal change (albeit local) must occur, since the sample suddenly breaks down after having been exposed to a *constant* external stress level for 25 minutes.

At this point, a full explanation of the permittivity's variation with DC bias voltage has not been realized. However, a significant fraction of the apparent magnitude increase can be explained by an actual increase in the vacuum capacitance of the foil electrodes, caused by the increased mechanical stress (and associated strain) on the dielectric foil,

$$\frac{|\Delta C_0|}{|C_0|} \approx \frac{\Delta d}{d_0} \approx \frac{\varepsilon_0}{E}\left(\frac{\varepsilon_\infty U_{DC}}{d_0}\right)^2 \approx 0.7\% \quad , \qquad (19)$$

where E is the elastic modulus of the foil. While the numerical value obtained is already in the right ballpark for explaining the observed increase in magnitude (~2.4%), there seems to be (at least) one

additional mechanism at work, as the increase of C_0 does not explain the change in the loss angle, as well as the frequency-dependence of the observed magnitude changes.

On the methodological side, the presented setup demonstrates the possibility of broadband high-voltage dielectric online monitoring down to a precision that is ultimately limited by the drift of the transfer functions over time (rather than the achievable instrument precision). This drift could however be taken into account by trading some of the current setup's simplicity. Indeed, by using a second, identically constructed current transformer that measures the current flowing through the capacitive divider (with the same settings of the prior sample measurement) one could limit the overall drift of the system to the drift of the divider capacitor and the differential drift of the two current transformers. The capacitance of the voltage divider is mainly determined by the high-voltage capacitor, for which a vacuum or gas type construction would be the preferred choice for lowest drift. Moreover, the measurement of *absolute* values of permittivity would then be possible (Equation 17).

The applied signal processing (analog integration of the current signal) is shown to be a simple solution for dealing with the challenge associated with the precise digitization of signals with large crest factors. We tested another, arguably even simpler approach, which consists of using a commercial low-noise *linear* amplifier in conjunction with a high-order low-pass filter with a cutoff frequency f_{LP} above the target frequency range. Then, only the harmonics in the target range contribute to the current peak and the crest factor is reduced by a factor of about f_c/f_{LP}, that is, to $CF_{I,LP} \approx 2f_{LP}\sqrt{T \cdot \tau_r}$. For example, using f_{LP}= 200 kHz reduces the crest factor of the current (for τ_r = 100 ns and T = 1ms) from 71 to about 4, which is close to the crest factor obtained with the integrator ($\lesssim$2). Either case is a variation on the theme of low-pass filtering, thus yielding comparable performance.

While in this study only rectangular waveforms with a fixed frequency (1 kHz) and duty cycle (50%) have been used, it is possible to synthesize and apply pulse-width-modulated binary signals with tailored frequency spectra [9]. The voltage excitation would then be switched (e.g. for a second every minute) from the stressing waveform to the scanning waveform, which covers the frequency range desired for the dielectric response analysis.

5 SUMMARY

This work merges and improves existing technologies to design a dielectric spectrometer that allows the quasi-continuous online monitoring of a specimen's dielectric spectrum under repetitive medium-voltage pulse stress. Limitations on switching speeds are removed by using analog integration of the current signal. Furthermore, a reference technique that eliminates the need for modelling transfer functions is proposed. It allows monitoring the time evolution of *relative changes* in the specimen's dielectric spectrum. This is useful information for dielectric aging studies, because the dielectric spectrum mirrors changes in the molecular structure, as well as the build-up of macroscopic dipoles from space charges.

ACKNOWLEDGMENTS

This project was carried out within the frame of the Swiss Centre for Competence in Energy Research on the Future Swiss Electrical Infrastructure (SCCER-FURIES) with the financial support of the Swiss Innovation Agency.

REFERENCES

[1] W.S. Zaengl, "Dielectric Spectroscopy in Time and Frequency Domain for HV Power Equipment", IEEE El. Ins. Magazine, Vol. 19, No. 5, pp. 5-19, 2003.

[2] R. Färber, C.M. Franck, "Modular High-Precision Dielectric Spectrometer for Quantifying the Aging Dynamics in (Sub-)Picofarad Polymeric Specimens", IEEE TDEI, Vol. 25, No. 3, pp. 1056-1063, 2018.

[3] P. Preetha, M.J. Thomas, "Life estimation of electrothermally stressed epoxy", IEEE TDEI, Vol. 21, No. 3, pp. 1154-1160, 2014.

[4] I. Semenov, C. Leu, "Loss factor and permittivity measurement at medium frequency high voltage with an HVDC offset", INSUCON 2017, Birmingham, UK.

[5] B. Sonerud, T. Bengtsson, J. Blennow, S.M. Gubanski, "Dielectric response measurements utilizing semi-square voltage waveforms", IEEE TDEI, Vol. 15, No. 4, pp. 920-926, 2008.

[6] R. Färber, T. Guillod, F. Krismer, J.W. Kolar, C.M. Franck, "Endurance of Polymeric Insulation under Mixed-Frequency Medium-Voltage Stress", to be published.

[7] R.A. Ion, "Nonparametric Statistical Process Control", Ph.D. Dissertation, University of Amsterdam, 2001.

[8] D.J. Sheskin, "Handbook of Parametric and Nonparametric Statistical Procedures", Taylor & Francis Ltd., 4th Edition, pp. 197-198.

[9] M. Min, J. Ojarand, O. Märtens, T. Paavle, R. Land, P. Annus, M. Rist, M. Reidla, T. Parve, "Binary Signals in Impedance Spectroscopy", Int. Conf. of the IEEE Engineering In Medicine and Biology Society, pp. 134-137, 2012.